applied sciences

MDPI

Article

On Thermodynamic Aspects of Oxide Crystal Growth

Detlef Klimm [1,*] and Nora Wolff [2]

[1] Leibniz-Institut für Kristallzüchtung, Max-Born-Str. 2, 12489 Berlin, Germany
[2] Helmholtz-Zentrum für Materialien und Energie, Hahn-Meitner-Platz 1, 14109 Berlin, Germany; nora.wolff@helmholtz-berlin.de
* Correspondence: detlef.klimm@ikz-berlin.de

Abstract: Several metal oxide compounds, especially those containing metals possessing several valence states, are able to absorb or release oxygen under suitable thermodynamic conditions. Such behavior is found often in systems containing oxides of transition metals. It is important to note that the equilibrium oxidation level of those metal oxides can depend on the aggregation state, which may significantly impede crystal growth processes from the melt. If during the melt growth of such oxide crystals, the average valence state of the oxides is different in the molten and solid state, then crystallization is connected with the absorption of free oxygen from the ambient gas, or with the release of free oxygen into it. This phenomenon can be detected by simultaneous DTA/TG measurements and can deteriorate the stability of crystal growth. This holds especially if the average valence in the solid is smaller than in the melt, because oxygen release can lead to bubble formation at the crystallization front.

Keywords: crystal growth; oxide; valence; bubble; phase diagram; gas phase; thermogravimetry (TG); differential thermal analysis (DTA)

Citation: Klimm, D.; Wolff, N. On Thermodynamic Aspects of Oxide Crystal Growth. *Appl. Sci.* **2022**, *12*, 2774. https://doi.org/10.3390/app12062774

Academic Editor: Victor Rouco

Received: 15 February 2022
Accepted: 3 March 2022
Published: 8 March 2022

1. Introduction

1.1. Oxide Bulk Crystal Growth

The first oxide material from which crystals were grown on an industrial scale is α-quartz (SiO_2). Quartz crystals are still of high technical relevance; their growth technique, as described in 1953 by Walker [1], relies on hydrothermal solutions. However, the equilibria between solvents and solutes will not be in the focus of this article. Rather, equilibria between oxides in the solid (crystalline) and molten state will be described, which are important for the growth of crystals from the melt, e.g., using the Czochralski, Bridgman, or float-zone methods [2,3]. Here, the Czochralski method is demonstrated first for $CaWO_4$, which is now often used for different materials such as $LiNbO_3$, YAG ($Y_3Al_5O_{12}$) and other garnets, and partially for α-Al_2O_3 (usually named sapphire, but "corundum" would be more accurate) [4]. These materials can be grown in different atmospheres, ranging from air to "pure" argon or nitrogen with ca. 99.9…99.999% purity. Independently of these different conditions, the constituent metal cations prevail almost completely in one oxidation state. Here, these are Ca^{2+}, W^{6+}, Li^{+}, Nb^{5+}, Y^{3+}, or Al^{3+}, respectively.

Some other substances, especially many transparent conducting oxides (TCO's), behave differently: crystals of β-Ga_2O_3 (melting point $T_f \approx 1800$ °C, [5]) and ZnO ($T_f = 1975$ °C, [6]) can be grown only if a sufficiently high oxygen partial pressure p_{O_2} prevails in the atmosphere. With current FactSage data [7] one calculates that at their melting points, Ga_2O_3 (sol/liq) is stable for $p_{O_2} \gtrsim 10^{-6}$ bar, and ZnO (sol/liq) for $p_{O_2} \gtrsim 5 \times 10^{-4}$ bar. If p_{O_2} falls below these limits, Ga^{3+} or Zn^{2+} is reduced to the corresponding metal, which occurs here in a gaseous state. On the other side, sufficiently high p_{O_2} will always stabilize Ga^{3+} or Zn^{2+} and, hence, Ga_2O_3 or ZnO because no higher oxidation state exists. The opposite holds for the melt growth of Ti^{3+} doped Al_2O_3 crystals ("Ti:sapphire") because Ti^{3+} is the lowest possible valence state of titanium under all conditions, where Al_2O_3 can be

grown from the melt. Hence, p_{O_2} should be as low as possible under realistic experimental conditions, e.g., by introducing graphite parts in the growth setup [8,9].

The situation is more complicated if an intermediate oxidation state is desired. This is the case, for example, for wüstite FeO and olivine $(Fe,Mg)_2SiO_4$ [10]—both containing Fe^{2+}. These phases are stable only in a corridor $p_{O_2}^{min}(T) < p_{O_2} < p_{O_2}^{max}(T)$, and the lower and upper limits rise with temperature T. It was demonstrated, however, that also under such conditions, "dynamic atmospheres" containing mixtures of CO_2 and CO often can deliver some $p_{O_2}(T)$, which stabilizes the desired oxidation state over a wide T range [11,12]. Thermogravimetric measurements with aegirine ($NaFe^{3+}Si_2O_6$) nanocatalysts showed mass losses up to 25% during heating to 700 °C in air. The mass loss decreased significantly if the material was doped with Ni^{2+}, which substitutes for Fe^{3+} as well as for Na^+. Even if such high mass loss results mainly from the desorption of volatiles from the surface, contributions of changing Fe valence are possible [13].

Several oxide materials with an intermediate oxidation state received attention as prospective ionic electrical conductors. In a series of publications, Han et al. demonstrated this for some mixed ionic–electronic conducting (MIEC) oxides. These oxides are typically based on the perovskite structure, or are derived from it by additional Ruddlesden–Popper-like layers in the crystal structure. Perovskites of the type $La_{0.6}Sr_{0.4}Co_{0.2}Fe_{0.8}O_{3-\delta}$, as hollow fibers, can separate oxygen from gas mixtures [14–16]. Ruddlesden–Popper-like phases such as Mo-doped Pr_2NiO_4 and $La_2Ni_{1-x}Mo_xO_{4+\delta}$ showed partially enhanced stability and efficiency in gas mixtures containing carbon dioxide [17,18].

This paper intends to show that, unfortunately, the stabilization of the desired oxidation state in the solid phase is sometimes insufficient for obtaining a stable growth process for bulk crystals. Problems can arise if significantly different oxidation states of metal ions prevail in the melt, and in the crystal which is grown from that melt. Calcium ferrite $Ca_2Fe_2^{3+}O_5$ is introduced in the following subsection as a paragon in detail, and some more examples are presented later in brief.

1.2. Calcium Ferrite as Model Substance

The orthorhombic "brownmillerite-like" crystal structure of calcium ferrite $Ca_2Fe_2O_5$ was described first by Bertaut [19] in the space group *Pcnm* with lattice parameters $a = 5.64$ Å, $b = 14.68$ Å, and $c = 5.39$ Å. The structure refinement by Berggren [20] used another setting *Pnma* of the same space group #62 with lattice parameters $a = 5.4253$ Å, $b = 14.7687$ Å, $c = 5.5980$ Å. In the structure, the Fe^{3+} ions are coordinated by O^{2-}, in alternately distorted tetrahedral and distorted octahedral environments, and form chains along the b axis. Figure 1 shows one unit cell, drawn with data from Redhammer et al. [21], where the chemical composition was found to be $Ca_{2.01\pm0.02}Fe_{2.00\pm0.01}O_5$. The structure is occasionally described as an ordered oxygen-deficient perovskite. One can take $a' = a/\sqrt{2}, b' = b/4, c' = c/\sqrt{2}$ as the lattice parameters for this slightly distorted ordered perovskite, and this structure was reported to be stable up to at least 1100 °C [22]. Recently, it was shown, however, that the structure is incommensurately modulated already at 827 °C [23]. It should be noted that the compound $Ca_2Fe_2O_5$ appears also as the mineral Srebrodolskite [24]. In the last years, $Ca_2Fe_2O_5$ received rising interest as a potential component of anodes in Li-ion batteries, as well as a catalyst for the steam-iron process to produce hydrogen [25,26].

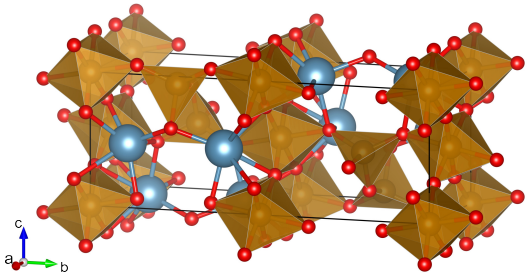

Figure 1. In the unit cell of $Ca_2Fe_2O_5$, Fe^{3+} ions in octahedral and tetrahedral coordination are alternating along the *b* axis. (Ca^{2+}—blue, O^{2-}—red) [21,27].

The formation of $Ca_2Fe_2O_5$ from powders of $CaCO_3$ and different iron oxides (FeO, Fe_3O_4, Fe_2O_3) was investigated by Jeon et al. [28]. Ceretti et al. [29] succeeded to grow $Ca_2Fe_2O_5$ single crystals of good quality from the melt by the optical float zone (OFZ) technique, which is a strong indication for congruent melting. For this growth method, a polycrystalline stoichiometric feed rod is moved through a hot zone, which is heated by the focused radiation of lamps; Cerreti et al. used two 500 W halogen lamps for heating. (More details for the OFZ method can be found elsewhere [3]). Increased oxygen mobility in the crystals above ca. 450 °C was observed by thermogravimetric (TG) measurements of ^{18}O enriched material in $^{16}O_2$ atmosphere. The observed mass loss was finished at ca. 600 °C and was attributed to the $^{18}O/^{16}O$ exchange. Congruent melting of $Ca_2Fe_2O_5$ in air or pure oxygen at 1449 °C was also observed by Phillips and Muan [30]; but in Figure 1 of their article, these authors presented also an alternative phase diagram CaO–Fe_2O_3, where this phase melts peritectically already at ca. 1435 °C under the release of solid CaO and an iron oxide rich melt.

In the following, thermoanalytic measurements and thermodynamic calculations for a x CaO + $(1-x)$ Fe_2O_x mixture with fixed composition $x = 0.700$ are presented. This is slightly more rich in CaO, compared to the $Ca_2Fe_2O_5$ phase ($x = 0.667$), and near the CaO/$Ca_2Fe_2O_5$ eutectic, which was reported by Phillips and Muan [30] at $x_{eut} = 0.673$ and $T_{eut} = 1438$ °C. Irrespective of whether $Ca_2Fe_2O_5$ shows congruent or incongruent melting, it is the major phase in solids with $x = 0.700$.

2. Experiments and Results

Simultaneous differential thermal analysis (DTA) and thermogravimetry (TG) was performed in a NETZSCH STA 449 F3 "Jupiter" with "type S" thermocouples and platinum crucibles using heating/cooling rates of ±10 K/min. The samples were prepared by mixing appropriate quantities of $CaCO_3$ and Fe_2O_3 powders of ≥99.99% purity in a mortar. To avoid charging errors, the metal oxide assay of both chemicals was preliminarily controlled as separate DTA/TG measurements [31].

The thermal analyzer establishes, via mass flow controllers, three independent gas flows that are unified in the sample chamber. The first "protective gas" flow was held constant at 20 mL/min argon, and to this were added either 50 mL/min Ar or 50 mL/min O_2, which sets an overall gas flow rate of 70 mL/min for all measurements. From this, one obtains for the latter measurements $p_{O_2} = (50/70)$ bar ≈ 0.71 bar. For the measurements in (20 + 50) mL/min Ar, the rest of the impurities of the nominally 99.999% pure Ar sets a lower limit, and can be estimated on a level of $p_{O_2} \approx (2 \times 10^{-6} \ldots 1 \times 10^{-5})$ bar in agreement with earlier investigations of the Fe–O system [10]. Equilibrium phase formation was performed in a first DTA/TG cycle, and the results of the second heating runs are shown in Figure 2.

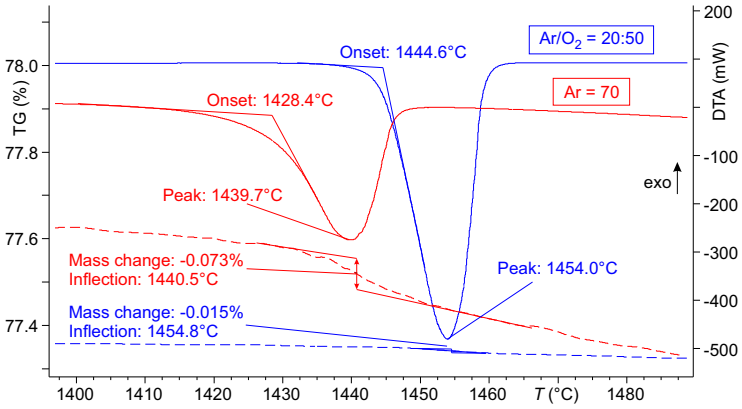

Figure 2. DTA (full lines) and TG (dashed lines) of CaO–Fe_2O_3 mixtures with 70% CaO. Sample masses were 65–70 mg, atmosphere was Ar (99.999% purity) or an Ar/O_2 mixture (flow rates given in mL/min.)

Both measurements show one endothermal DTA melting peak which is broader, and is shifted to lower T in the "pure" Ar atmosphere. In both cases, the melting process is accompanied by a mass loss which is marginal (0.015%) in the oxygen-rich atmosphere and almost five times larger in Ar. The inflection points in both TG curves are in fairly good agreement with the endothermal minimum positions of the DTA curves. This means that the melting process is obviously directly related to the mass loss.

The experimental results are confirmed by the FactSage [7] calculations that are shown in Figure 3. These curves were obtained by calculating the equilibria between the starting mixture of CaO and Fe_2O_3 (1 mole in total) in an excess of the corresponding atmosphere (7 mole gas in total) in 1 K steps. In both cases, $Ca_2Fe_2O_5$ is the dominating solid phase at 1380 °C, accompanied by a smaller amount of Fe-saturated CaO, which is designated in the following as CaO(ss). $Ca_2Fe_2O_5$ is known as a stoichiometric line compound without significant variation of the oxygen stoichiometry [29]. Hence, the small iron content (a few percent, [32]) in the minority phase CaO(ss) is expected to be the only carrier of Fe^{2+} in the solids.

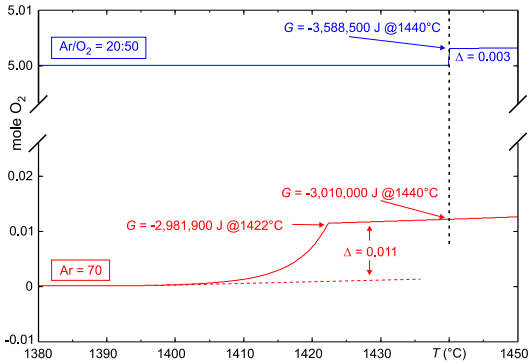

Figure 3. Calculated equilibrium of 0.7 mol CaO + 0.3 mol Fe_2O_3 in 5 mol O_2 + 2 mol Ar, or in 7 mol Ar, respectively. The curves show the total amount of O_2 in the atmosphere. Total Gibbs energy G of the system given at selected points.

The situation is different for the liquid phase, where under accessible conditions, always an equilibrium between Fe^{2+} and Fe^{3+} prevails. From the Ellingham diagrams of the Fe–O_2 system (cf. [10,33]) it is obvious that the liquid FeO_x "slag" phase always contains both valence states of iron, and their ratio depends on T and p_{O_2}. Gurry and Darken [34] measured in a CaO/FeO_x melt with 36.6 mol-% CaO that was held for 1 h at 1574 °C a Fe^{3+}/Fe^{2+} ratio of ≈19. Recently, Bykova et al. [35] showed that even under very high temperatures, $T \gg 2000$ K and pressures $p > 50$ GPa Fe_2O_3 does not melt stoichiometrically; rather, mixed valence oxides of a series nFeO·$m$$Fe_2O_3$ were found.

Solid Fe_2O_3 will convert under ambient pressure to a molten phase between ≈1500…1600 °C, under the release of oxygen. This process can be described as a chemical reaction

$$\underbrace{m\,Fe^{3+} + \frac{3m}{2}\,O^{2-}}_{=m\,FeO_{1.5}} \rightleftarrows (m-n)\,Fe^{3+} + \frac{3m-n}{2}\,O^{2-} + n\,Fe^{2+} + \frac{n}{4}\,O_2\uparrow \quad (1)$$

and it is obvious that the amount of Fe^{2+} which is formed during this melting process depends on p_{O_2} in the surrounding atmosphere. This is confirmed by the lower experimental mass loss for the blue TG curve in Figure 2, and is in agreement with the calculated smaller oxygen release for the blue curve in Figure 3.

The vertical dashed line in Figure 3 marks $T = 1440$ °C, where in both cases, the whole system is molten. At the melting points (1422 °C for the red curve, 1440 °C for the blue curve), G for the solid and liquid phases is identical. At 1440 °C, G is more negative for the blue curve, because there, iron remains also in the melt, preferably as Fe^{3+}. For the red curve, partial reduction according to Equation (1) takes place, which is endothermal. At this temperature, the reduction of 1 mole pure Fe_2O_3 requires 346,840 J. This major contribution is supplemented other effects (e.g., different specific heat capacity), which are not treated here in detail.

3. Discussion

3.1. Calcium Ferrite

The DTA curves in Figure 2 show that the sample melts in Ar at lower T than in the Ar/O_2 mixture. The melting peak is broader in the oxygen deficient gas flow. Fortunately, reliable thermodynamic data on the Ca–Fe–O ternary system are available, e.g., from the assessment by Hillert et al. [32]. Under the given experimental conditions, only calcium iron(III) ferrites are stable because calcium iron(II,III) ferrites, such as $CaFe_3O_5$ ("CWF"), are formed only for lower p_{O_2}, e.g., in atmospheres containing hydrogen [36]. The samples with 70% CaO that were used in Figure 2 contain CaO(ss) as the second solid phase, as indicated above.

The melting point of CaO (≈2900 °C) is far above the melting point of $Ca_2Fe_2O_5$, and correspondingly, the eutectic point between both phases is very close to the latter compound. This leads to interesting results if one calculates the phase equilibria between the end members Fe_2O_3 and CaO under different p_{O_2}.

Both graphs in Figure 4 should not be labeled "phase diagrams" because the end members are not able to form all intermediate phases—in this case, Fe_3O_4. The upper panel (a) was calculated for a constant $p_{O_2} = 0.71$ bar, which corresponds to the flow of 20 mL/min Ar + 50 mL/min O_2. Here, three intermediate calcium iron(III) ferrites exist, and $Ca_2Fe_2O_5$ melts congruently at 1445 °C. The extrapolated onset of the blue melting peak of the 70% mixture in Figure 2 is very close to this melting point, and to the eutectic temperature at 1440 °C. (The small difference cannot be resolved in the DTA curve.) It is interesting to note that the "Fe_2O_3+slag" phase field on the left side extends only to ca. 1440 °C because at higher T, the iron(II,III) oxide Fe_3O_4 is formed.

It is not possible to give exact data for the oxygen partial pressure that prevails during the measurements in "pure" argon. The value $p_{O_2} = 1 \times 10^{-5}$ bar that was used for the calculation of Figure 4b should be considered a lower limit, which is delivered by the contamination of the Ar gas of nominally 99.999% purity with air. However, additional oxygen could be added by minor leaks of the DTA apparatus, or by gases emanating from the sample itself, such as CO_2 from the calcination of $CaCO_3$.

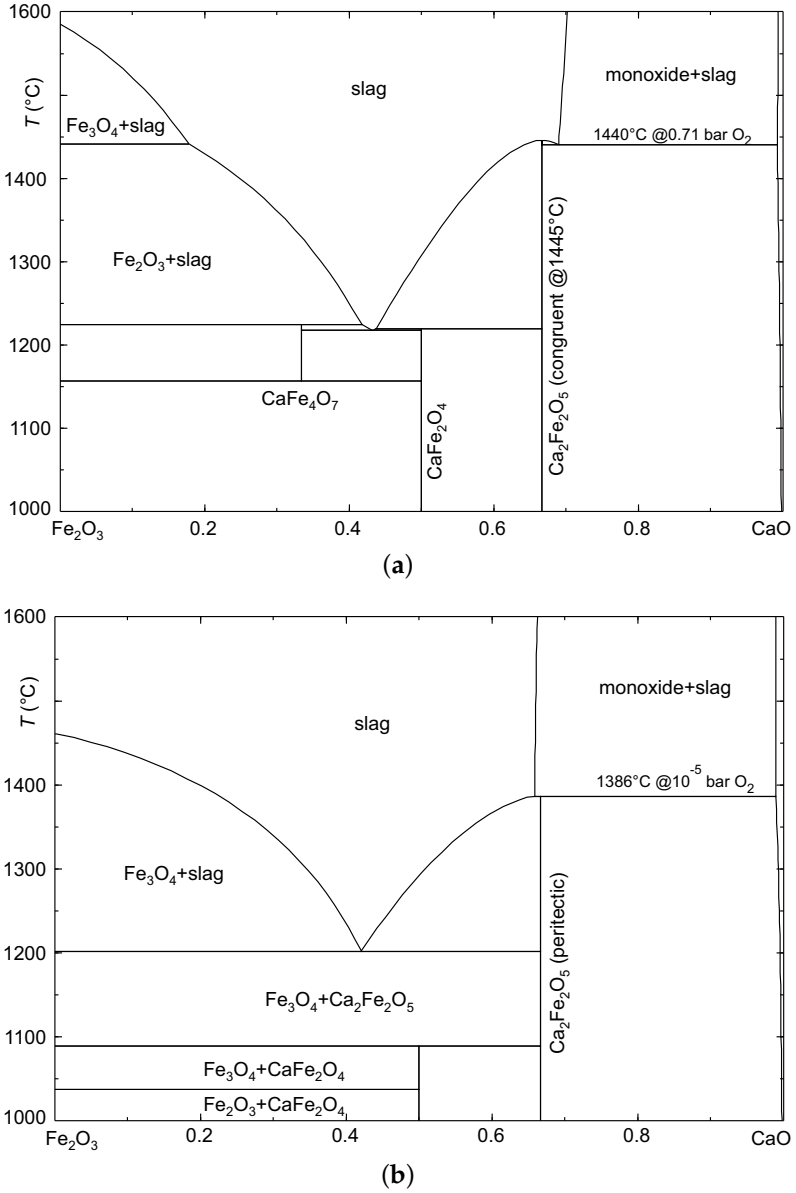

Figure 4. Isopleth sections CaO–Fe_2O_3 of the system FeO–Fe_2O_3–CaO, calculated for different atmospheres with FactSage [7]. (**a**) Calculation for $p_{O_2} = 0.71$ bar: $Ca_2Fe_2O_5$ melts congruently, and the eutectic toward CaO is at $T_{eut} = 1440$ °C. (**b**) Calculation for $p_{O_2} = 1 \times 10^{-5}$ bar: $Ca_2Fe_2O_5$ melts incongruently under the release of CaO(ss) at $T_{inc} = 1386$ °C.

The stability range of the $CaFe_4O_7$ phase, which contains a high amount of Fe^{3+}, is very limited already for 0.71 bar oxygen pressure (Figure 4a, [32]). Under the significantly lower p_{O_2} in Figure 4b, this phase is not stable at all, and also the highest temperature, where both calcium iron(III) ferrites are stable, is decreased. For $Ca_2Fe_2O_5$, this results in incongruent melting under the release of CaO(ss), and the melting process can be described by a reaction

$$Ca_2Fe_2O_5 \rightleftarrows 2\,CaO + \left(1 - \frac{x}{2}\right) Fe_2O_3 + x\,FeO + \frac{x}{4}\,O_2 \uparrow \quad (2)$$

which relates the mass loss $\frac{x}{4}\,O_2$ to the amount of x FeO in the melt. For the red TG curve in Figure 2, showing a mass loss of 0.073% upon melting, one calculates with Equation (2) $x = 0.025$. This means that ≈1.2% of the iron ions are reduced to Fe^{2+}. This is significantly

less than that measured by Gurry and Darken (≈5%, [34]). However, they performed the following:

- These authors equilibrated samples at 1574 °C, which is 130 K higher than the onset of the melting peak shown in Figure 2. Higher T, however, shifts the redox equilibrium Equation (1) to the product side.
- Their CaO/FeO_x melt contained only 36.6% CaO, but the CaO concentration of the samples in this study was on the same CaO/FeO_x scale at 53.8%. The higher CaO content is known to stabilize Fe^{3+} [30].

3.2. Other Examples

Reversible mass changes during the melting and crystallization of oxide compounds were reported occasionally in the literature:

- The rare-earth calcium oxyborates $YCa_4O(BO_3)_3$ and $GdCa_4O(BO_3)_3$ gain 0.009% or 0.014% mass, respectively, upon melting in air [37].
- If mixtures of MoO_3 and V_2O_5 are molten together, a phase $6\,MoO_3 \cdot 0.5\,V_2O_4 \cdot 4\,V_2O_5 = V_9Mo_6O_{40}$ is formed, which contains V^{4+} and V^{5+}. If the mixtures are molten in air, the mass rises due to oxidation of V^{4+} to V^{5+}. The reverse effect occurs during crystallization. If molten or cooled in Ar, the mass remains constant [38,39]. It should be noted that also in some A_2BO_4-type materials, molybdenum plays a role in oxygen storage and transport [17,18].
- The color of $SrPrGaO_4$ (SPG) crystals depends sensitively on the growth atmosphere. Only if the atmosphere is virtually free of O_2, or if grown crystals are annealed under reducing conditions (e.g., in forming gas), the crystals are green from Pr^{3+}. Already, several ppm O_2 result in dark red/brownish coloring. It seems that the darker color is related to partial oxidation to Pr^{4+}; however, this explanation is disputed. Nevertheless, incorporation of interstitial oxygen is proven. With simultaneous DTA/TG measurements, it was found that melting is accompanied by a positive TG step, and the magnitude of this step ($\lesssim$0.2%) is almost proportional to the oxygen concentration in the atmosphere during the measurement [40,41].
- Recently Wolff et al. reported crystal growth experiments from the melt with delafossite-type crystals $Cu^{+}Me^{3+}O_2$ (Me = Al, Fe) [42,43]. It turned out that only small millimeter-sized crystallites of $CuAlO_2$ could be obtained. The experiments with $CuFeO_2$, in contrast, were more successful, and single crystalline OFZ bars with diameters up to 10 mm and several centimeters in length were obtained. It is shown in the next section that this very different behavior of isotype crystals with similar melting temperatures around 1200 °C results from the different oxidation levels of the ions in the liquid and solid phases: the melts contain in both cases Cu^{+} and Cu^{2+}, and both solids only Cu^{+}. This requires the reduction in Cu^{2+} ions during crystallization. The valence state of Al^{3+} does not change during the crystallization of $CuAlO_2$. For $CuFeO_2$, in contrast, the melt contains besides the incorporated Fe^{3+} also significant amounts of Fe^{2+} which must be oxidized.
- More recently, it was shown that also during the crystallization of $Bi_2^{3+}Cu^{2+}O_4$ and $Bi_2^{3+}Pd^{2+}O_4$, the mass rises, due to oxygen incorporation and partial oxidation of Cu^{+} or Pd^{0} to the two-valent state. Bi_2CuO_4 single crystals up to 6 mm in diameter and 7 cm in length were obtained by OFZ [44].

4. Conclusions

Many transition metals can occur in a variety of oxidation states, depending on the oxygen concentration in the atmosphere and on temperature. Molten oxides usually contain more than one of these oxidation states because the simultaneous occurrence of several valences favors the mixture entropically. In contrast, solids contain often (but not always) only one valence for each element.

If during oxide crystal growth from the melt, the average valence states in the melt and in the crystal are different, free oxygen molecules must be either absorbed from the

ambient gas, or must be released. Taking this into account, the terms "congruent melting" and "peritectic melting" become disputable: "congruent melting" means in the closer sense that the solid and the melt in equilibrium possess an identical chemical composition; and "peritectic melting" means that a solid converts, upon heating, to a melt with a different composition under the release of another solid. In both cases, the gas phase should not, per definition, be involved. However, changing the valence of ions requires involvement of the gas phase. In particular, the exchange of O_2 with the gas phase can lead to bubbles, which destabilize or inhibit crystal growth [45–49].

Figure 5a demonstrates this for the case where the average oxidation level of the crystal is higher, compared to the melt. Continuously, the melt must absorb O_2(gas) from the atmosphere to facilitate the Me^n/Me^{n+1} equilibrium in the melt, because the latter ion is permanently incorporated into the crystal. Possibly, this limits the maximum growth rate, but nevertheless, the growth of crystals with a high oxidation state, such as the initial example $Ca_2Fe_2O_5$ [29], or Bi_2CuO_4 [44], is possible without severe problems.

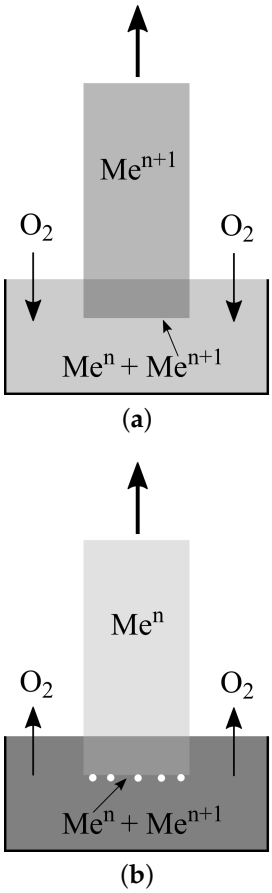

Figure 5. Growth of a metal oxide crystal with integer valence of the metal Me from a melt with different valences, Me^n and Me^{n+1}. A darker color means a higher oxidation level. (**a**) The crystal contains the higher valence $(n+1)$ and only Me^{n+1} is incorporated from the melt. The melt depletion by this ion must be compensated by the oxidation of Me^n ions. (**b**) The crystal contains the lower valence (n) and only Me^n is incorporated from the melt. The melt depletion by this ion must be compensated by a reduction in Me^{n+1} ions, under the production of free oxygen. This will occur preferably at the crystallization front, and can lead there to bubbles (white circles).

Figure 5b shows the opposite case where the average oxidation level of the crystal is lower than that of the melt. During growth, Me^n is incorporated into the crystal, and readjustment of the Me^n/Me^{n+1} equilibrium in the melt requires permanent reduction in the latter. Melt depletion by Me^n will occur at the crystallization front, and consequently, the formation of O_2 gas bubbles is expected there. The volume of these bubbles can be

estimated from Equation (1): the reduction in 1 mole Me^{n+1} to Me^{n} produces $\frac{1}{4}$ moles O_2. Assuming an ideal gas, this corresponds to, for example, 1700 K to as much as 35 litres. In the case of iron (atomic mass 55.8 g/mol), every gram of reduced iron delivers ≈ 630 mL O_2 at this temperature. Wolff et al. described recently "almost peritectic" melting processes, where a solid phase decomposes to a melt and another solid phase under the compulsive exchange with the gas phase, as "exaperitectic", derived from the Greek $\varepsilon\xi\alpha\tau\mu\iota\sigma\eta$ (to exhaust).

As a conclusion, it is recommended to adjust (if possible) the atmosphere for crystal growth experiments with critical valence changes during crystallization in such a way that these changes between the solid and liquid phases remain small, e.g., by reactive components, such as CO_2 [11]. The measurement of mass changes during melting/crystallization in a simultaneous DTA/TG measurement is a useful tool to detect such critical valence changes.

Author Contributions: Conceptualization, D.K.; investigation, N.W. and D.K.; writing, D.K. and N.W. All authors have read and agreed to the published version of the manuscript.

Funding: This research received no external funding.

Institutional Review Board Statement: This article has passed the institutional review board procedure of Leibniz-Institut für Kristallzüchtung (IKZ) Berlin, Germany.

Acknowledgments: The authors are indebted to Zbigniew Galazka for reading the manuscript.

Conflicts of Interest: The authors declare no conflict of interest.

References

1. Walker, A.C. Hydrothermal synthesis of quartz crystals. *J. Am. Ceram. Soc.* **1953**, *36*, 250–256. [CrossRef]
2. Sarukura, N.; Nawata, T.; Ishibashi, H.; Ishii, M.; Fukuda, T. Czochralski growth of oxides and fluorides. In *Handbook of Crystal Growth*, 2nd ed.; Rudolph, P., Ed.; Elsevier: Boston, MA, USA, 2015; pp. 131–168. doi: 10.1016/B978-0-444-63303-3.00004-3. [CrossRef]
3. Dabkowska, H.A.; Dąbkowski, A.B.; Hermann, R.; Priede, J.; Gerbeth, G. Floating zone growth of oxides and metallic alloys. In *Handbook of Crystal Growth (Second Edition)*; Rudolph, P., Ed.; Elsevier: Boston, MA, USA, 2015; pp. 281–329. [CrossRef]
4. Brandle, C.D. Czochralski growth of oxides. *J. Cryst. Growth* **2004**, *264*, 593–604. [CrossRef]
5. Tomm, Y.; Reiche, P.; Klimm, D.; Fukuda, T. Czochralski grown Ga_2O_3 crystals. *J. Cryst. Growth* **2000**, *220*, 510–514. [CrossRef]
6. Klimm, D.; Ganschow, S.; Schulz, D.; Fornari, R. The growth of ZnO crystals from the melt. *J. Cryst. Growth* **2008**, *310*, 3009–3013. [CrossRef]
7. GTT Technologies, Kaiserstr. 100, 52134 Herzogenrath, Germany. FactSage 8.1. 2021. Available online: http://www.factsage.com/ (accessed on 1 October 2021).
8. Uecker, R.; Klimm, D.; Ganschow, S.; Reiche, P.; Bertram, R.; Roßberg, M.; Fornari, R. Czochralski growth of Ti:sapphire laser crystals. *Optically Based Materials and Optically Based Biological and Chemical Sensing for Defence II*; International Society for Optics and Photonics (SPIE): Bellingham, WA, USA, 2005; Volume 5990, pp. 53–61. [CrossRef]
9. Xuan, L. Thermodynamic and Kinetic Model of Point Defect Distributions during Ti:sapphire Growth. Ph.D. Thesis, SIMaP-INP-UGA, Grenoble, France, 2021.
10. Klimm, D.; Ganschow, S. The control of iron oxidation state during FeO and olivine crystal growth. *J. Cryst. Growth* **2005**, *275*, e849–e854. [CrossRef]
11. Klimm, D.; Ganschow, S.; Schulz, D.; Bertram, R.; Uecker, R.; Reiche, P.; Fornari, R. Growth of oxide compounds under dynamic atmosphere composition. *J. Cryst. Growth* **2009**, *311*, 534–536. [CrossRef]
12. Ganschow, S.; Schulz, D.; Klimm, D.; Bertram, R.; Uecker, R. Application of predominance diagrams in melt growth of oxides. *Cryst. Res. Technol.* **2010**, *45*, 1219–1224. [CrossRef]
13. Sebakhy, K.O.; Vitale, G.; Pereira-Almao, P. Dispersed Ni-doped aegirine nanocatalysts for the selective hydrogenation of olefinic molecules. *ACS Appl. Nano Mater.* **2018**, *1*, 6269–6280. [CrossRef]
14. Han, N.; Zhang, C.; Tan, X.; Wang, Z.; Kawi, S.; Liu, S. Re-evaluation of $La_{0.6}Sr_{0.4}Co_{0.2}Fe_{0.8}O_{3-\delta}$ hollow fiber membranes for oxygen separation after long-term storage of five and ten years. *J. Membr. Sci.* **2019**, *587*, 117180. [CrossRef]
15. Han, N.; Zhang, W.; Guo, W.; Xie, S.; Zhang, C.; Zhang, X.; Fransaer, J.; Liu, S. Novel oxygen permeable hollow fiber perovskite membrane with surface wrinkles. *Sep. Purif. Technol.* **2021**, *261*, 118295. [CrossRef]
16. Han, N.; Shen, Z.; Zhao, X.; Chen, R.; Thakur, V.K. Perovskite oxides for oxygen transport: Chemistry and material horizons. *Sci. Total Environ.* **2022**, *806*, 151213. [CrossRef] [PubMed]

17. Han, N.; Wei, Q.; Zhang, S.; Yang, N.; Liu, S. Rational design via tailoring Mo content in $La_2Ni_{1-x}Mo_xO_{4+\delta}$ to improve oxygen permeation properties in CO_2 atmosphere. *J. Alloys Compds.* **2019**, *806*, 153–162. [CrossRef]
18. Han, N.; Guo, X.; Cheng, J.; Liu, P.; Zhang, S.; Huang, S.; Rowles, M.R.; Fransaer, J.; Liu, S. Inhibiting in situ phase transition in Ruddlesden-Popper perovskite via tailoring bond hybridization and its application in oxygen permeation. *Matter* **2021**, *4*, 1720–1734. [CrossRef]
19. Bertaut, E.F.; Blum, P.; Sagnières, A. Structure du ferrite bicalcique et de la brownmillerite. *Acta Cryst.* **1959**, *12*, 149–159. [CrossRef]
20. Berggren, J. Refinement of the crystal structure of dicalcium ferrite, $Ca_2Fe_2O_5$. *Acta Chem. Scand.* **1971**, *25*, 3616–3624. [CrossRef]
21. Redhammer, G.J.; Tippelt, G.; Roth, G.; Amthauer, G. Structural variations in the brownmillerite series $Ca_2(Fe_{2-x}Al_x)O_5$: Single-crystal X-ray diffraction at 25 °C and high-temperature X-ray powder diffraction (25 °C$\leq T \leq$ 1000 °C). *Am. Mineral.* **2004**, *89*, 405–420. [CrossRef]
22. Shin, S.; Yonemura, M.; Ikawa, H. Crystallographic properties of $Ca_2Fe_2O_5$. Difference in crystallographic properties of brownmillerite-like compounds, $Ca_2Fe_2O_5$ and $Sr_2Fe_2O_5$, at elevated temperatures. *Bull. Chem. Soc. Jpn.* **1979**, *52*, 947–948. [CrossRef]
23. Krüger, H.; Kahlenberg, V. Incommensurately modulated ordering of tetrahedral chains in $Ca_2Fe_2O_5$ at elevated temperatures. *Acta Cryst. B: Struct. Sci.* **2005**, *61*, 656–662. [CrossRef]
24. Chesnokov, B.V.; Bazhenova, L.F. Srebrodolskite $Ca_2Fe_2O_5$—A new mineral. *Zap. VseSoyuznogo Mineral. Obshchestva* **1985**, *114*, 195–199. Available online: https://rruff.info/uploads/ZVMO114N2_195.pdf (accessed on 1 October 2021). (In Russian)
25. Sharma, N.; Shaju, K.M.; Subba Rao, G.V.; Chowdari, B.V.R. Mixed oxides $Ca_2Fe_2O_5$ and $Ca_2Co_2O_5$ as anode materials for Li-ion batteries. *Electrochim. Acta* **2004**, *49*, 1035–1043. [CrossRef]
26. Chan, M.S.C.; Liu, W.; Ismail, M.; Yang, Y.; Scott, S.A.; Dennis, J.S. Improving hydrogen yields, and hydrogen:steam ratio in the chemical looping production of hydrogen using $Ca_2Fe_2O_5$. *Chem. Eng. J.* **2016**, *296*, 406–411. [CrossRef]
27. Momma, K.; Izumi, F. VESTA 3 for three-dimensional visualization of crystal, volumetric and morphology data. *J. Appl. Cryst.* **2011**, *44*, 1272–1276. [CrossRef]
28. Jeon, J.; Jung, S.M.; Sasaki, Y. Formation of calcium ferrites under controlled oxygen potentials at 1273 K. *ISIJ Int.* **2010**, *50*, 1064–1070. [CrossRef]
29. Ceretti, M.; Corallini, S.; Paulus, W. Influence of phase transformations on crystal growth of stoichiometric brownmillerite oxides: Sr_2ScGaO_5 and $Ca_2Fe_2O_5$. *Crystals* **2016**, *6*, 146. [CrossRef]
30. Phillips, B.; Muan, A. Phase equilibria in the system CaO–iron oxide in air and at 1 atm. O_2 Pressure. *J. Amer. Ceram. Soc.* **1958**, *41*, 445–454. [CrossRef]
31. Bertram, R.; Klimm, D. Assay measurements of oxide materials by thermogravimetry and ICP-OES. *Thermochim. Acta* **2004**, *419*, 189–193. [CrossRef]
32. Hillert, M.; Selleby, M.; Sundman, B. An assessment of the Ca–Fe–O system. *Met. Trans. A* **1990**, *21*, 2759–776. [CrossRef]
33. Klimm, D. *Thermal Analysis and Thermodynamics in Materials Science*; De Gruyter STEM: Berlin, Germany, 2022.
34. Gurry, R.W.; Darken, L.S. The composition of CaO–FeO–Fe_2O_3 and MnO–FeO–Fe_2O_3 melts at several oxygen pressures in the vicinity of 1600°. *J. Amer. Chem. Soc.* **1950**, *72*, 3906–3910. [CrossRef]
35. Bykova, E.; Dubrovinsky, L.; Dubrovinskaia, N.; Bykov, M.; McCammon, C.; Ovsyannikov, S.V.; Liermann, H.P.; Kupenko, I.; Chumakov, A.I.; Rüffer, R.; Hanfland, M.; Prakapenka, V. Structural complexity of simple Fe_2O_3 at high pressures and temperatures. *Nat. Commun.* **2016**, *7*, 10661. [CrossRef]
36. Berger, C.M.; Mahmoud, A.; Hermann, R.P.; Braun, W.; Yazhenskikh, E.; Sohn, Y.J.; Menzler, N.H.; Guillon, O.; Bram, M. Calcium-iron oxide as energy storage medium in rechargeable oxide batteries. *J. Am. Ceram. Soc.* **2016**, *99*, 4083–4092. [CrossRef]
37. Klimm, D.; Bertram, R.; Ganschow, S.; Doerschel, J. Phase separation in oxide-borate mixed systems. *J. Chem. Eng. Data* **2003**, *48*, 120–123. [CrossRef]
38. Slade, R.C.T.; Ramanan, A.; West, B.C.; Prince, E. The structure of $V_9Mo_6O_{40}$ determined by powder neutron diffraction. *J. Solid State Chem.* **1989**, *82*, 65–69. [CrossRef]
39. Klimm, D.; Orlinski, K.; Pawlak, D.A. Self-organized V–Mo oxide fibers by the micro-pulling down method. *Mater. Res. Soc. Symp. Proc.* **2010**, *1223*, 1209–1223. [CrossRef]
40. Uecker, R.; Reiche, P.; Ganschow, S.; Uecker, D.C.; Schultze, D. Investigation of crystal growth of $SrPrGaO_4$ and $SrLaGaO_4$. *Acta Phys. Pol. A* **1997**, *92*, 23–34. [CrossRef]
41. Pajaczkowska, A.; Novoselov, A.; Klimm, D.; Talik, E.; Uecker, R. Does valency of Pr ions influence color of $SrPrGaO_4$ single crystals? *Cryst. Growth Des.* **2004**, *4*, 497–501.+. [CrossRef]
42. Wolff, N.; Klimm, D.; Siche, D. Thermodynamic investigations on the growth of $CuAlO_2$ delafossite crystals. *J. Solid State Chem.* **2018**, *258*, 495–500. [CrossRef]
43. Wolff, N.; Schwaigert, T.; Siche, D.; Schlom, D.G.; Klimm, D. Growth of $CuFeO_2$ single crystals by the optical floating-zone technique. *J. Cryst. Growth* **2020**, *532*, 125426. [CrossRef]
44. Wolff, N.; Klimm, D.; Habicht, K.; Fritsch, K. Crystal growth and thermodynamic investigation of $Bi_2M^{2+}O_4$ (M = Pd, Cu). *CrystEngComm* **2021**, *23*, 3230–3238. [CrossRef]
45. Nielsen, J.W.; Blank, S.L. Crystal growth and phase equilibrium studies in the system $(R.E.)_2O_3$–Fe_2O_3. *J. Cryst. Growth* **1972**, *13–14*, 702–705. [CrossRef]

46. Shimura, F.; Fujino, Y. Crystal growth and fundamental properties of $LiNb_{1-y}Ta_yO_3$. *J. Cryst. Growth* **1977**, *38*, 293–302. [CrossRef]
47. Behr, G.; Löser, W.; Apostu, M.O.; Gruner, W.; Hücker, M.; Schramm, L.; Souptel, D.; Teresiak, A.; Werner, J. Floating zone growth of CuO under elevated oxygen pressure and its relevance for the crystal growth of cuprates. *Cryst. Res. Technol.* **2005**, *40*, 21–25. [CrossRef]
48. Li, Q.J.; Xu, L.M.; Fan, C.; Zhang, F.B.; Lv, Y.Y.; Ni, B.; Zhao, Z.Y.; Sun, X.F. Single crystal growth of the pyrochlores $R_2Ti_2O_7$ (R = rare earth) by the optical floating-zone method. *J. Cryst. Growth* **2013**, *377*, 96–100. [CrossRef]
49. Wizent, N.; Leps, N.; Behr, G.; Klingeler, R.; Büchner, B.; Löser, W. The effect of process parameters on floating zone crystal growth of selected cuprates. *J. Cryst. Growth* **2014**, *401*, 596–600. [CrossRef]